

Tebaldini, S., d'Alessandro, M. M., Ulander, L. M. H., Bennet, P., Gustavsson, A., Coccia, A., Macedo, K., Disney, M., Wilkes, P., Spors, H.-J., Schumacher, N., Hanuš, J., Novotný, J., Brede, B., Bartholomeus, H., Lau, A., van der Zee, J., Herold, M., Schuettemeyer, D., Scipal, K. (2023): TomoSense: A unique 3D dataset over temperate forest combining multi-frequency mono- and bi-static tomographic SAR with terrestrial, UAV and airborne lidar, and in-situ forest census. - Remote Sensing of Environment, 290, 113532.

<https://doi.org/10.1016/j.rse.2023.113532>

1 **TomoSense: a unique 3D dataset over temperate forest combining multi-frequency mono-**
2 **and bi-static tomographic SAR with terrestrial, UAV and airborne lidar, and in-situ**
3 **forest census**

4
5 **Stefano Tebaldini¹, Mauro Mariotti d'Alessandro¹, Lars M.H. Ulander^{2,3}, Patrik Bennet², Anders**
6 **Gustavsson³, Alex Coccia⁴, Karlus Macedo⁴, Mathias Disney⁵, Phil Wilkes⁵, Hans-Joachim Spors⁶,**
7 **Nico Schumacher⁶, Jan Hanuš⁷, Jan Novotný⁷, Benjamin Brede^{8,9}, Harm Bartholomeus⁸, Alvaro**
8 **Lau⁸, Jens van der Zee⁸, Martin Herold^{8,9}, Dirk Schuettemeyer¹⁰, Klaus Scipal¹⁰**

- 9 1. Dipartimento di Elettronica, Informazione e Bioingegneria, Politecnico di Milano, Italy
10 2. Chalmers University of Technology, Sweden
11 3. Swedish Defence Research Agency (FOI), Sweden
12 4. MetaSensing, The Netherlands
13 5. University College London, Gower Street, London, UK; and NERC National Centre for Earth
14 Observation (NCEO), UCL, London, UK.
15 6. Landesbetrieb Wald und Holz Nordrhein-Westfalen, Germany
16 7. The Czech Academy of Sciences, Global Change Research Institute (CzechGlobe), Czech
17 Republic
18 8. Wageningen University & Research, Laboratory of Geo-Information Science and Remote
19 Sensing, Droevendaalsesteeg 3, 6708 PB Wageningen, The Netherlands
20 9. Helmholtz Center Potsdam GFZ German Research Centre for Geosciences, Section 1.4
21 Remote Sensing and Geoinformatics, Telegrafenberg, 14473 Potsdam, Germany
22 10. European Space Agency, European Union

23
24 Corresponding author

25 Stefano Tebaldini

26 Dipartimento di Elettronica, Informazione e Bioingegneria

27 Politecnico di Milano

28 Via Ponzio 34/5
29 20133, Milano
30 Italy
31 Tel: +39 02 2399 3614 Fax: +39 02 2399 3664
32 Email: stefano.tebaldini@polimi.it
33

34 **Abstract**

35 The TomoSense experiment was funded by the European Space Agency (ESA) to support research on
36 remote sensing of forested areas by means of Synthetic Aperture Radar (SAR) data, with a special focus
37 on the use of tomographic SAR (TomoSAR) to retrieve information about the vertical structure of the
38 vegetation at different frequency bands. The illuminated scene is the temperate forest at the Eifel
39 National Park, North-West Germany. Dominant species are beech and spruce trees. Forest height ranges
40 roughly from 10 to 30 m, with peaks up to over 40 m. Forest Above Ground Biomass (AGB) ranges
41 from 20 to 300 Mg/ha, with peaks up to over 400 Mg/ha. SAR data include P-, L-, and C-band surveys
42 acquired by flying up to 30 trajectories in two headings to provide tomographic imaging capabilities.
43 L- and C-band data were acquired by simultaneously flying two aircraft to gather bistatic data along
44 different trajectories.

45 The SAR dataset is complemented by 3D structural canopy measurements made via terrestrial laser
46 scanning (TLS), Unoccupied Aerial Vehicle lidar (UAV-L) and airborne laser scanning (ALS), and in-
47 situ forest census. This unique combination of SAR tomographic and multi-scale lidar data allows for
48 direct comparison of canopy structural metrics across wavelength and scale, including vertical profiles
49 of canopy wood and foliage density, and per-tree and plot-level above ground biomass (AGB). The
50 resulting TomoSense data-set is free and openly available at ESA for any research purpose. The data-
51 set includes ALS-derived maps of forest height and AGB, forest parameters at the level of single trees,
52 TLS raw data, and plot-average TLS vertical profiles. The provided SAR data are coregistered, phase
53 calibrated, and ground steered, to enable a direct implementation of any kind of interferometric or
54 tomographic processing without having to deal with the subtleties of airborne SAR processing.
55 Moreover, the data-base comprises SAR tomographic cubes representing forest scattering in 3D both
56 in Radar and geographical coordinates, intended for use by non-Radar experts. For its unique features
57 and completeness, the TomoSense data-set is intended to serve as an important basis for future research
58 on microwave scattering from forested areas in the context of future Earth Observation missions.

59

60 **1. Introduction**

61 The introduction of Synthetic Aperture Radar (SAR) tomography has opened the way to new
62 opportunities for microwave remote sensing of forested areas from space (Reigber and Moreira, 2000;
63 Tebaldini et al., 2019). Tomographic SAR surveys require illumination from multiple trajectories to
64 form a data-stack containing multiple SAR images of the same area. The data-stack is then digitally
65 processed to produce a collection of voxels that represent the backscattered energy in three dimensions,
66 thus allowing direct imaging of the interior of the illuminated media (Tebaldini et al. 2017). Space
67 Agencies have increasingly invested in SAR tomography in the last few years, funding activities to
68 assess the use of SAR tomography in the context of spaceborne remote sensing (Aghababaei, 2020;
69 Bloomberg et al., 2021; Tello et al., 2018; Toraño Caicoya et al., 2015; Pardini et al., 2018; Mariotti
70 and Tebaldini, 2019; Kathi et al., 2019; Ho Tong Minh et al., 2014 and 2016; Frey et al., 2008;
71 Fatoyinbo et al., 2021; El Moussawi et al., 2019). As a token of its potential, SAR tomography has been
72 assigned a dedicated 14-month acquisition phase in the context of the forthcoming Earth Explorer
73 mission BIOMASS, to be launched in 2024, (Quegan et al., 2019; Soja et al., 2021), and it has largely
74 been considered in the context of future bistatic missions operating at L-band (Azcueta and Tebaldini,
75 2020; Moreira et al., 2015; Scipal and Davidson, 2017).

76 In this context, the TomoSense experiment was organized by the European Space Agency (ESA) to
77 provide the scientific community with unprecedented data to study the features of radar scattering from
78 temperate forests, comprising tomographic and fully polarimetric SAR surveys at P-, L-, and C-band,
79 acquired in mono- and bistatic mode by simultaneously flying two aircraft. The dataset is complemented
80 by a range of dedicated datasets that have proven value in the estimation of above ground biomass
81 (AGB): a detailed forest census, terrestrial laser scanning (TLS) (Disney et al., 2018), mobile laser
82 scanning (MLS) (Mokroš et al., 2021), unoccupied aerial vehicle laser scanning (UAV-LS) (Brede et
83 al., 2017; Brede et al., 2022) and airborne laser scanning (ALS) products (Brovkina et al., 2022).”.

84 In this paper, we provide a comprehensive overview of the TomoSense experiment and the produced
85 data. The dataset is intended to serve as a basis for future research on microwave scattering from
86 forested areas, as it allows addressing applications such as retrieval of forest height and biomass,
87 along with studying the roles of species diversity and forest vertical structure. The dataset is intended

88 to be usable without requiring in-depth knowledge of SAR processing, and is freely and openly
89 available through ESA for research purposes

90 2. The Test site

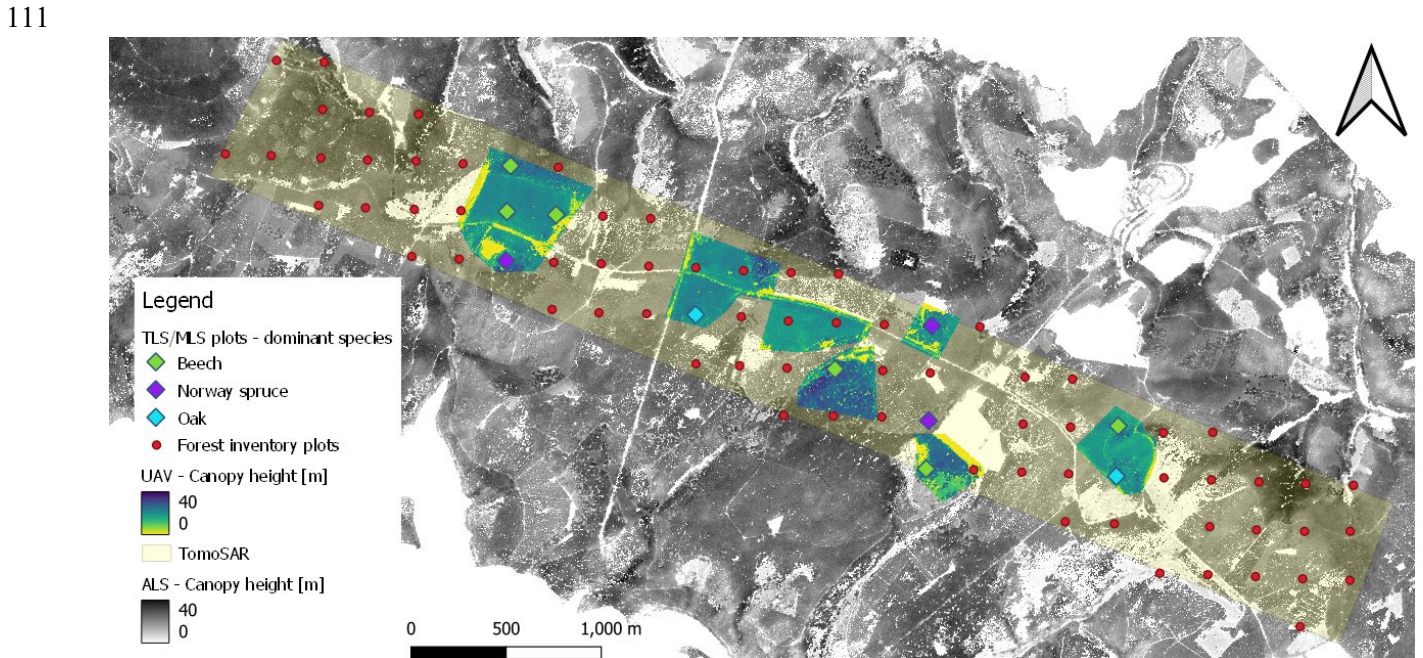
91 The test site of TomoSense is located within the Kermeter area in the Eifel National Park in North
92 Rhine-Westphalia, Germany. The site was chosen for its ecological diversity with forest stands of
93 different species, topography and age classes. In addition, being part of a National Park the site is well
94 documented and has an established forest census. The Kermeter is an upland region, up to 528 m above
95 sea level, covered by one of the largest contiguous, deciduous forests in that region. It covers an area of
96 3,592 hectares, of which about 3,300 hectares is a single forested area (the so-called Kermeter-
97 Hochwald or Kermeter High Forest). Beech woods dominate the shaded, damp northern slopes (24%),
98 in places with trees that are over 200 years old. Oak woods hold sway on the drier, southern slopes
99 (26%), interrupted by rocky outcrops (Felsheide). About 550 hectares consist of spruce trees, which are
100 a consequence of reforestation measures after the Second World War. However, the spruce stock is
101 continuously being reduced by thunderstorms, drought and bark beetle infestations in favour of
102 deciduous woods. A photo of the area is shown in figure 1. The Urft Valley in front / south of the
103 Kermeter was shaped by the meandering Urft River. In 1905 the construction of the Urft Dam was
104 finished and created an Amazon-like reservoir

105



106 **Fig. 1.** The Urft Valley in front / south of the Kermeter area at the Eifel National park, North-West
107 Germany.

108 The main area of interest targeted by all campaign activities is the one enclosed in the yellow rectangle
109 in figure 2. The area is approximately 6.4 Km long and 800 m wide. Topographic slopes at this area are
110 typically on the order of $\pm 5^\circ$, with few areas reaching 10° and beyond.



112
113 **Fig. 2.** Graphical overview of the TomoSense campaign.

114
115 **3. Forest census**

116 Forest census was carried out in spring 2019 to collect several tree parameters. Each parameter was
117 measured at single tree level within 80 plots with size of 0.05 ha (circular plot with radius 12.62 m).
118 The plots are from the permanent inventory established by Wald und Holz in 2011, see figure 2. The
119 distance between any two plots is about 250 m. Each plot centre is marked with a 40 cm long iron nail,
120 and the tree positions are a function of their angle and distance to the plot centre. The position of each
121 plot centre was measured using a Trimble Catalyst DA1 Antenna, which is expected to be accurate to
122 within 1 m. The combination of plot size (500m^2) and grid size represents a good compromise between
123 workload and statistical accuracy. At the same time, it allows the use of SAR airborne data to investigate
124 forest structure at the level of a single plot.

126 Field data include a total of 2564 sampled trees. For each of these, the following parameters were
127 collected:

- 128 o Tree position w.r.t. plot center;
- 129 o Diameter at Breast Height (DBH) in mm;
- 130 o Height in m;
- 131 o Species (ID and name);
- 132 o Number of trees per ha;
- 133 o Basal area;
- 134 o Basal area per hectare.

135 The data-set is complemented by photographic material including two photos of each plot, see figure 3.

136 In addition an area wide map on the dominant species is available form Wald and Holz.



Landscape

Portrait

137

138 **Fig. 3.** Landscape and portrait photos of plot 1330 (beech-oak forest).

139

140

141 4. Terrestrial Laser Scanning (TLS)

142 Collection of TLS data took place in September 2021. The campaign took place under nearly ideal

143 weather conditions with no wind. TLS data were acquired for 11 50 m x 50 m plots. Data was acquired

144 following a standardized protocol (Wilkes et al. 2017) where scans were acquired on a 16.7 m grid.
145 Individual scans were co-registered using reflective targets, so that the resulting combined plot-level
146 point cloud was accurate to within a few mm. Following co-registration, extraction of individual trees
147 was carried out by applying the workflow TLS2trees (Wilkes et al. 2022) based on semantic
148 classification approach, (Krisanski et al. 2021), that uses deep learning to classify a point cloud into
149 leaf, wood, coarse woody debris and ground points. The deep learning model is applied ‘as is’ i.e. no
150 additional pre-training is required Figure 4 shows the result of applying the TLS2trees workflow to
151 TLS data from plot 1330.

152



153

154

155 **Fig. 4.** Trees extracted from the TLS survey of plot 1330.

156

157 Following the individual tree extraction, tree volume was estimated using the TreeQSM (version 2.3.1)
158 (Raumonen et al. 2013). AGB at the level of single trees was then obtained based on published values
159 of wood density taken from (Zianis et al., 2005). An allometric model of the form $a(D^2H)^b$ was fitted
160 to the TLS-derived estimates of biomass, where D and H are tree diameter at breast height (DBH) and
161 height respectively. This model is a generic allometric form for tree volume and biomass estimation
162 that has been used for deciduous European woodland (Wutzler et al. 2008) as well as more widely
163 (Zianis et al, 2005). The resulting model was calibrated against the TLS-derived volume of 748 trees in
164 total, covering the dominant species, across a wide size range, and at different growth stages). The

165 model takes the form $1.131(D^2H)^{0.857}(r^2 = 0.96)$ and this subsequently used for the ALS-derived
166 estimates of AGB.

167 **4.1 Mobile Laser Scanning (MLS)**

168 MLS data were collected during the TLS campaign in September 2021 and all TLS plots were covered.
169 In contrast to TLS, where only few scan positions are visited, MLS systems are carried through the plot
170 and thereby view the canopy from this trajectory. MLS acquisition time is much faster than TLS on the
171 one hand. However, on the other hand, the range and power of these systems is often limited leading to
172 high occlusion in the upper canopy. At each plot, data were collected with a Greenvalley LiBackpack
173 DGC50 in two successive walks. The raw ranging and Inertial Measurement Unit (IMU) data were
174 processed with the provided Greenvalley software suite and resulting point clouds were registered to
175 world coordinates based on the UAV-LS point clouds.

176

177 **5. UAV Laser Scanning (UAV-LS)**

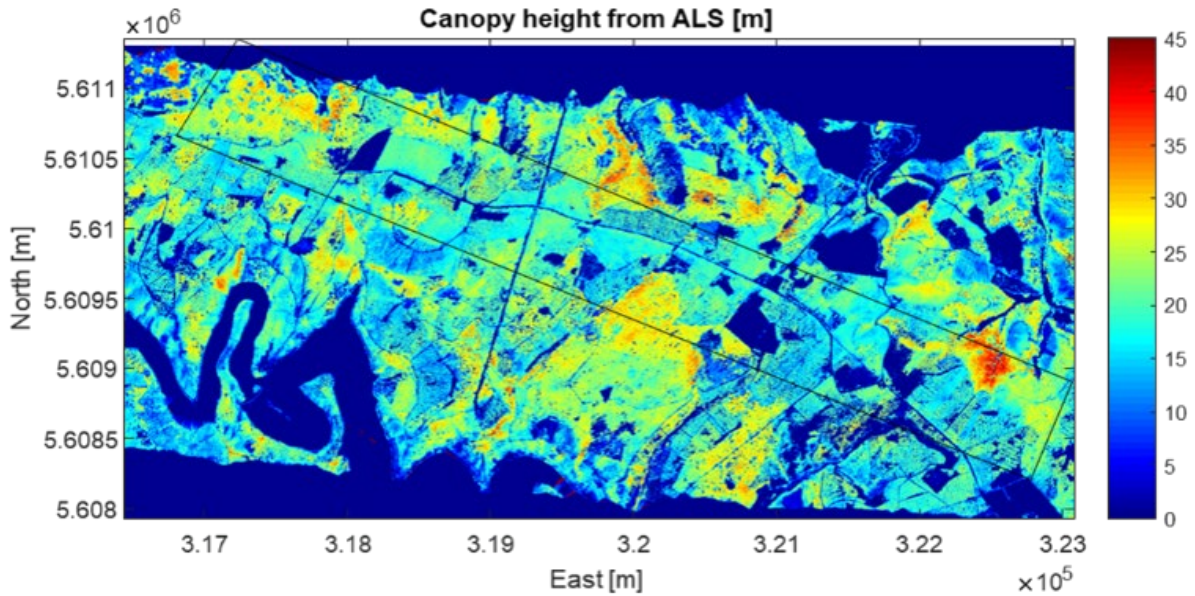
178 UAV-LS data were acquired alongside the TLS data in September 2021. Two primary modes of
179 acquisition were followed: first, coverage of all TLS plots in high density, cross-line patterns using one
180 flight per plot. Second, flights that covered complete stands where the TLS plots were located (see
181 figure 2). All flights were performed with a RIEGL VUX-1UAV and processing of raw sensor data to
182 point clouds followed standardized procedures (Brede et al., 2017).

183

184 **6. Airborne Laser Scanning (ALS)**

185 Small footprint lidar ALS data were acquired by CzechGlobe in summer 2018 and remeasured in
186 summer 2021. Lidar-derived products include terrain topography, forest height, and AGB estimates.
187 Lidar-derived forest height is shown in figure 5.

188



189

190 **Fig. 5.** Canopy Height Model (CHM) as derived from ALS data.

191

192 Spatial maps of forest AGB were produced by CzechGlobe based on data from the 80 forest census
 193 plots and corresponding AGB estimates derived using allometric equations based on analysis of TLS
 194 data (as described in section 4). The analysis was complemented by including information from
 195 additional 100 forest census plots from a previous study in the Silesian Beskids area at the border
 196 between Czech Republic and Poland, which is characterized by a similar species composition as in
 197 Kermeter. This choice was made to extend the biomass variability towards the low end, which is not
 198 well represented in Kermeter. Afterwards, plot data were partitioned into a training and validation sets,
 199 and used to train the coefficients of a number of predictors derived from ALS data through machine
 200 learning techniques (Brovkina et al., 2022). The top ten best performing models were averaged and the
 201 final robust meta-model was applied on predictors extracted in a regular grid to produce an AGB map
 202 in 10 m resolution.

203

204 7. SAR flights

205 SAR acquisitions were carried out by MetaSensing in July 2020 (P-band), September 2020 (L-band)
 206 and in November 2020 and October 2021 (C-band). All data were acquired by flying up to 30 times
 207 along two opposite headings (North-West and South-East), to provide vertical resolution capabilities

208 from two opposite views. L- and C-band data were acquired in bistatic mode by flying two identical
209 SAR sensors onboard two aircraft. In so-doing, we obtained for each flight heading a mono-static (same
210 sensor operated as transmitted and receiver) and a bi-static (one sensor as transmitter and the other as
211 receiver) data-set. All data were collected in fully polarimetric mode, resulting in the collection of
212 approximately one thousand SAR images.

213 All flights were performed using one or two Cessna 208 Grand Caravan, see figure 6, equipped with
214 GPS antennas and a power supply panel. SAR calibration was supported with two 5 m trihedral
215 reflectors for P-band installed by FOI, and two 75 cm ones for higher frequencies.

216



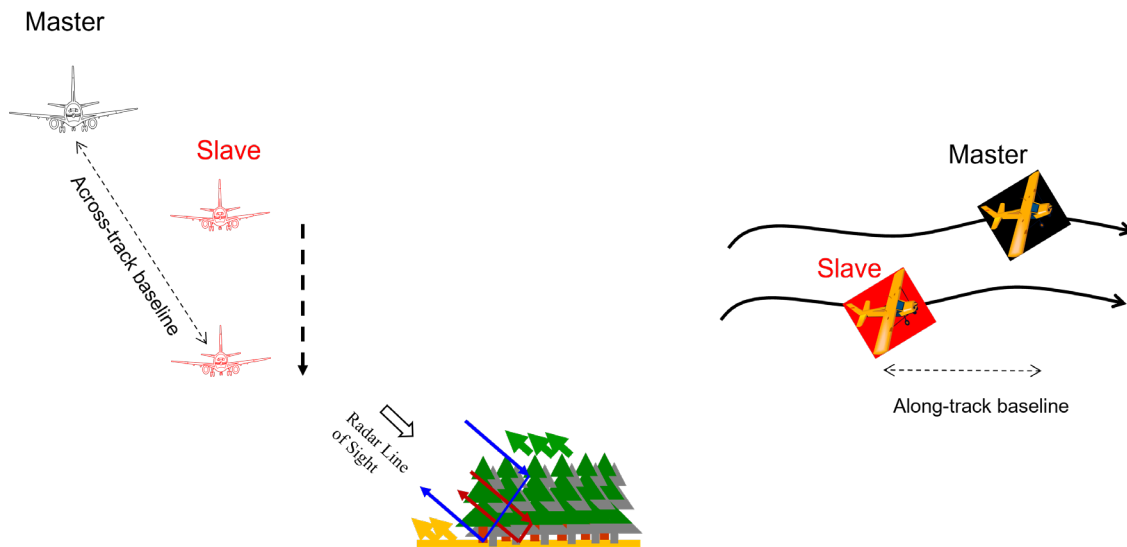
217

218 **Fig. 6.** The two Cessna 208 Grand Caravan used for the SAR flights.

219

220 P-Band trajectories were flown with constant altitude for the first 10 passes, and by progressively
221 lowering the trajectory in the subsequent 10 passes. Trajectories at L- and C-Band were planned so that
222 the second aircraft (Slave) follows the first one (Master) at a safe distance, reducing its altitude
223 progressively at each flight. The relative position of the Slave aircraft w.r.t. the Master is referred to in
224 jargon as *baseline*, and is commonly described in terms of its along-track and across-track components,
225 as represented in figure 7.

226



227

228 **Fig. 7.** Tomographic baselines. Master height is approximately 2000 m above the test site.

229

230 Unfortunately, the flight formation described above was not exactly implemented in 2020, resulting in
231 the across-track baselines to be substantially larger than planned. At L-Band, the impact of large
232 baselines was mitigated by the long wavelength, resulting in several single-pass interferograms where
233 the signal associated with forest scattering is clearly detected and can be used for tomographic analysis.

234 This was not the case at C-Band, and it was decided to fully re-fly the trajectories in October 2021 to
235 ensure the presence of properly small and large baselines.

236 In all bistatic flights, safety conditions did not allow to fly at the planned along-track distance of 20 m.
237 This resulted in an actual along-track distance between the two aircraft ranging from 50 m to 150 m,
238 corresponding to a net delay between the images acquired by the two aircraft ranging from 0.5 s to 1.5
239 s. Relevant data parameters are summarized in Table 1 below.

240

241

242

243

244

	P-Band	L-Band	C-Band
Polarization	Full-pol	Full-pol	Full-pol
Bandwidth	30 MHz	50 MHz	100 MHz
Along-track resolution	≈ 1 m	≈ 1 m	≈ 0.6 m
Flight heading	North-West and South-East	North-West and South-East	North-West and South-East
Number of passes per heading	28 monostatic	30 monostatic 30 bistatic	17 monostatic 17 bistatic
Vertical resolution in the main area of interest	≈ 5 m to 10 m	< 5 m	< 5 m
Bistatic along track baseline	Not applicable	50 to 150 m	50 to 150 m

245 **Table 1.** Summary of SAR data

246
247

8. SAR processing and derived products

248 Radar processing was aimed at producing “tomographic cubes”, i.e.: 3D voxels representing the
249 complex scattering coefficients in 3D, with the height direction being relative to terrain topography
250 (Tebaldini et al. 2017). To achieve this goal, several processing steps were needed.

251 In the first place, SAR data acquired along any single flight were focused by MetaSensing) directly in
252 ground-coordinates, using terrain topography derived from ALS data and information about the
253 platform trajectory from navigational data. The focusing processor corrects for amplitude factors related
254 to distance variations and the antenna radiation pattern, in such a way as to directly associate image
255 intensity with the backscatter coefficient (σ^0) in all polarizations. Despite that, however, the data had
256 to be re-calibrated polarimetrically to fix some inconsistent features ascribed to the Radar system, which
257 showed up mostly as offsets affecting the polarimetric phase and magnitudes in different flights. This
258 problem was interpreted as being related to triggering and stopping the acquisition in each pass.

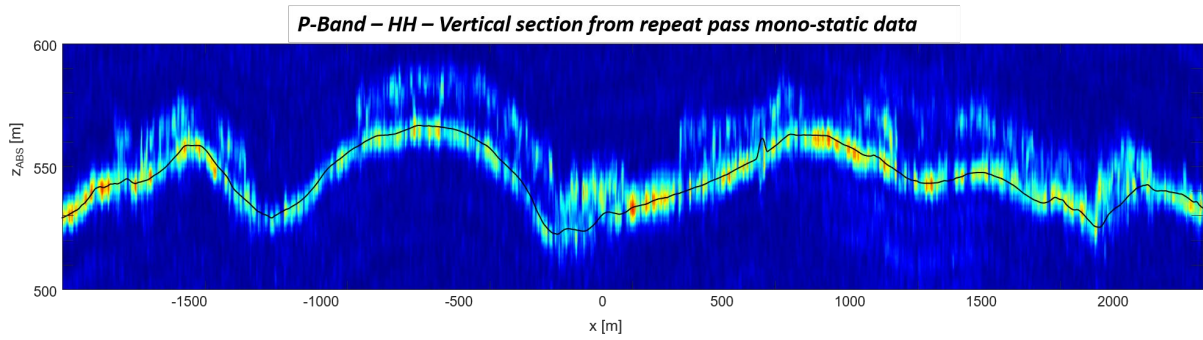
259 Accordingly, it was corrected under the assumption of a single distortion matrix per overpass, following
260 the approach in (Villa et al., 2015). Afterwards, the polarimetric signature appeared to be uniform across
261 all passes, and consistent with the expected features of forested areas.
262 Subsequent processing activities consisted in interferometric calibration and 3D focusing. As in most
263 interferometric and tomographic campaigns, large part of calibration activities was aimed at correcting
264 for mispositioning and phase errors due to inaccuracies of navigational data on the scale of a fraction
265 of a wavelength (Tebaldini et al., 2016). This result was achieved in two steps. The first step consisted
266 in the correction of azimuth shifts between different images, which was implemented following the
267 multi-squint procedure proposed in (Reigber et al., 2006). The second calibration step was necessary to
268 finely correct unwanted residual phase terms due to residual motion, which was implemented following
269 the phase center double localization approach in (Tebaldini et. al, 2016). Calibrated SAR images were
270 processed as described in (Yu et al., 2020) to generate 3D tomographic cubes. For an evaluation of the
271 resulting imaging quality we refer the reader to section 8.1.

272

273 **8.1 Tomographic imaging**

274 We report a few examples to comment on the quality of TomoSense tomographic data. Figure 8 shows
275 a tomographic transect, or *tomogram*, of the Kermeter forest as obtained by taking a vertical section
276 from a P-Band tomographic cube (North-West heading, HH) and normalizing such that the sum over
277 height is unitary for visualization purposes. The tomogram is visibly well focused, as it allows for a
278 clear detection of the forest canopies and its lower envelope is very well correlated with ALS terrain
279 topography (black line). The same transect is shown at HH and HV polarization in figure 9, where the
280 vertical axis is now relative to ALS terrain elevation (i.e.: terrain topography is found at 0 m in each
281 column). It is evident that the upper envelope of both tomograms is in very good agreement with ALS
282 canopy height (white line). Interestingly, one can observe that ground scattering is dominant at HH,
283 whereas canopy scattering is better detected at HV, consistently with observations in other forest biomes
284 (Tebaldini et al., 2019).

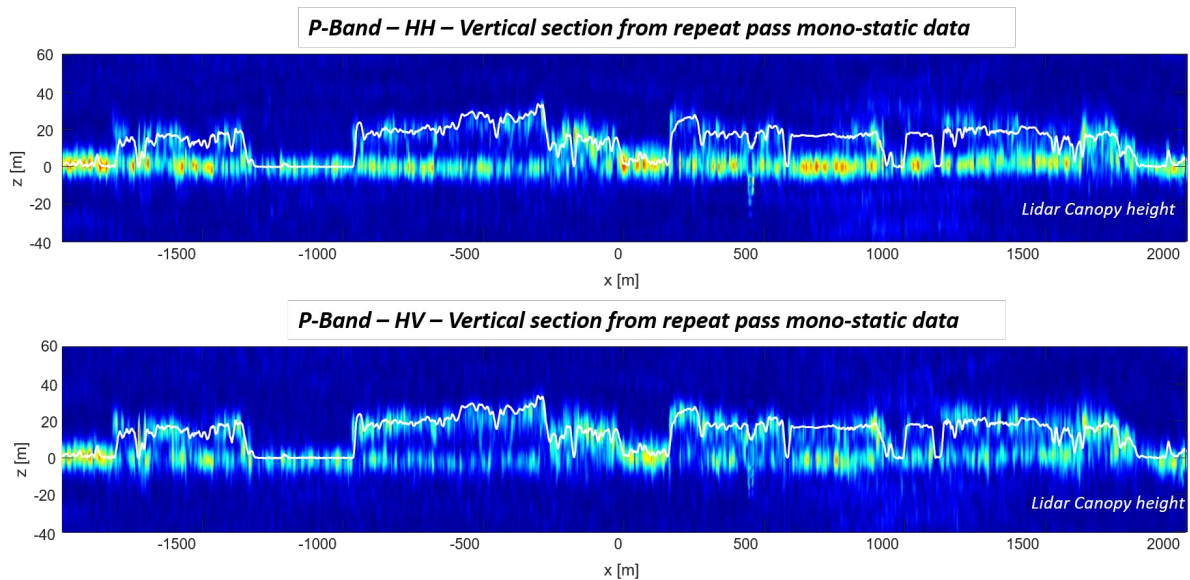
285



286

287 **Fig. 8.** P-Band tomography: vertical section (HH) in absolute coordinates. The black line overlaid
 288 denotes terrain topography from ALS data.

289



290

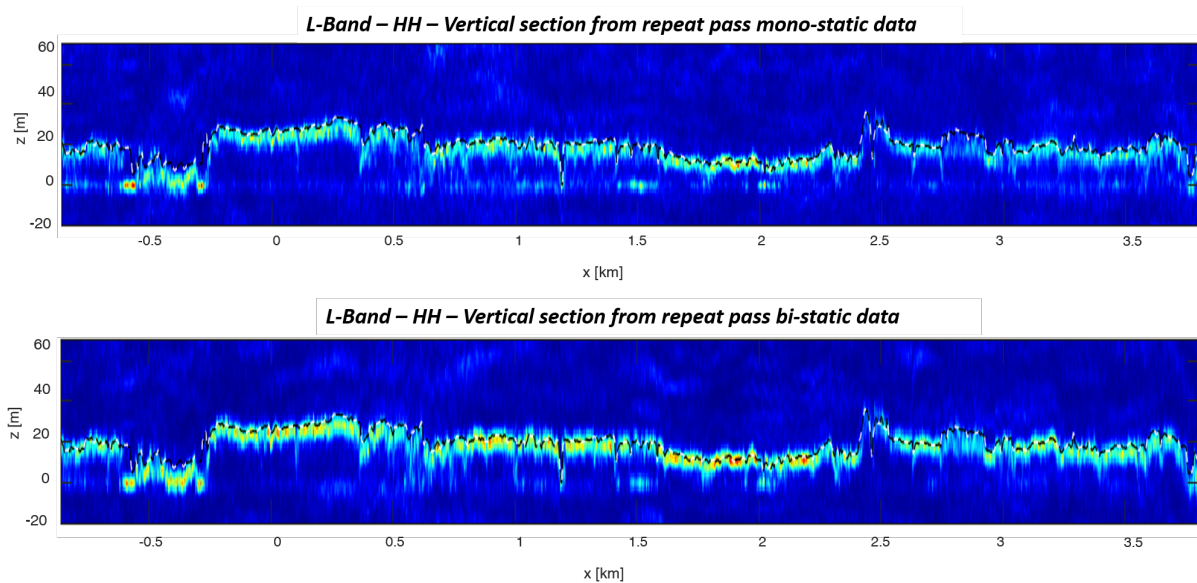
291 **Fig. 9.** P-Band tomography: vertical sections (HH and HV) w.r.t. terrain elevation (i.e.: terrain
 292 topography is found at 0 m in each column). The white lines overlaid denotes canopy height from ALS
 293 data.

294

295 L-band mono- and bi-static tomograms are shown in figure 10. Canopy scattering is dominant as
 296 compared to P-Band, consistent with the physics of forest scattering. It is interesting to note that
 297 scattering from the terrain level (at 0 m in figure 10) is weaker in the case of bi-static data (quantitative
 298 analysis on the whole area shows an average decrease of about 4 dB w.r.t. mono-static data). This is
 299 consistent with the finding in (Mariotti et al., 2013) that scattering from the ground level is largely

300 contributed by double-bounce interactions between the trunks and the terrain, resulting in large part of
 301 the scattered energy to return to the transmitter.

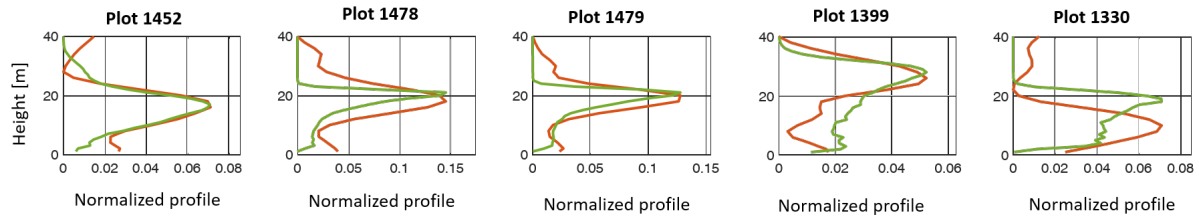
302 Figure 11 shows a comparison between L-Band bistatic Tomography and TLS at five plots sampled by
 303 with TLS. TLS data are represented by the average Plant Area Volume Density (PAVD), associated
 304 with the green curves, whereas tomographic data are represented by the average profile and are
 305 associated with the red curves. TLS and TomoSAR profiles are observed to exhibit a good agreement,
 306 especially for plots 1452, 1478, 1479. In plot 1399, the main peak is correctly detected by TomoSAR,
 307 but the understory seems to be underestimated w.r.t. to the TLS profile. Viceversa, the top of the
 308 canopy is not detected by TomoSAR in plot 1330. Such discrepancies are to be ascribed to the use of
 309 radically different wavelength and vertical resolution. Another factor to account for is that the graphs
 310 in figure 11 are only representative of the average profiles within each plot, whereas more information
 311 could be retrieved by analysing the spatial variability of TomoSAR vertical profiles, as in (Pardini et
 312 al., 2018b).



313

314 **Fig. 10.** L-Band tomography: vertical sections (mono-static and bistatic) w.r.t. terrain elevation. The
 315 dashed lines overlaid denotes canopy height from ALS data.

316

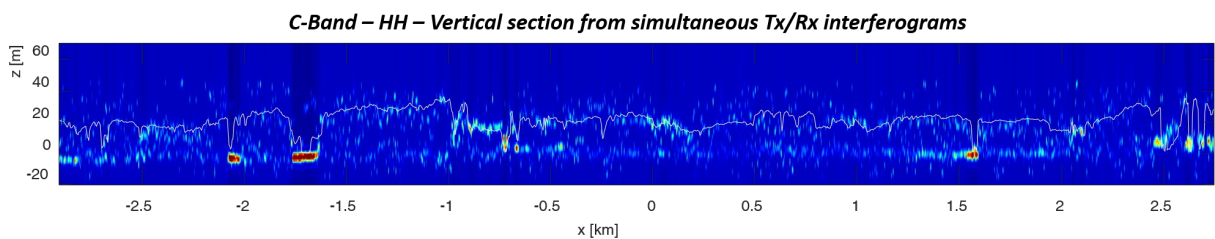


317

318 **Fig. 11.** Comparison between TLS and SAR Tomography at the five plots. Green curves: Plant Area
 319 Volume Density (PAVD, m^2/m^3) from TLS. Red curves: normalized tomographic profile from bistatic
 320 HV L-Band data (average over each plot).

321

322 Differently from L-Band, the signal from canopy scattering could not be detected in C-Band repeat pass
 323 data due to temporal decorrelation resulting from the time elapsed between consecutive flights (on the
 324 order of few minutes). A partial detection of the forest canopies is achieved by processing only image
 325 pairs acquired in the same pass (Tebaldini and Ferro-Famil, 2017), see figure 12. In this case, temporal
 326 decorrelation is only induced by the time lag between mono- and bi-static images from the same flight,
 327 which is slightly larger than the decorrelation time of canopy scattering at C-Band (Monteith and
 328 Ulander, 2022). Interestingly, the ground signal is here well detected, which demonstrates some
 329 penetration capabilities at C-Band as well.



330

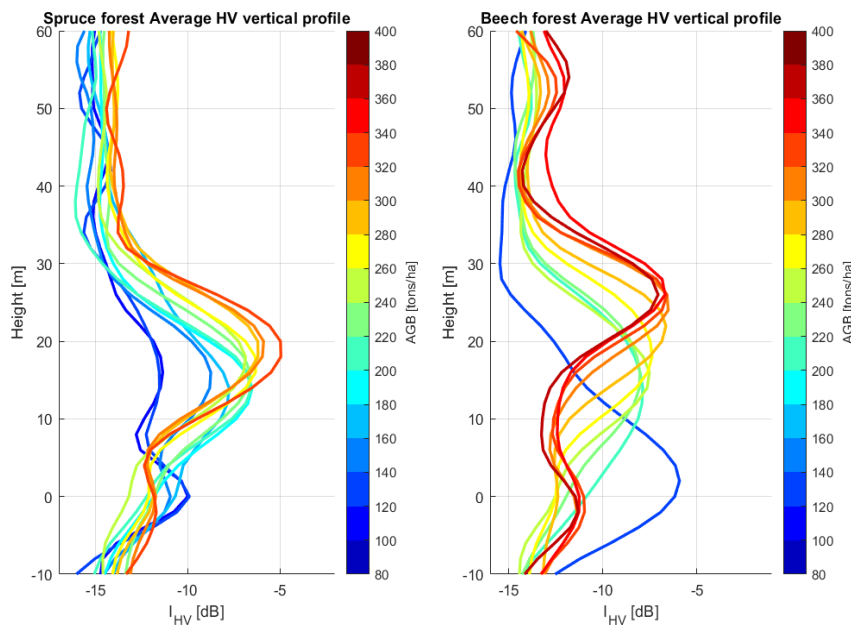
331 **Fig. 12.** C-Band tomography: vertical sections w.r.t. terrain elevation. The white lines overlaid denotes
 332 canopy height from ALS data.

333

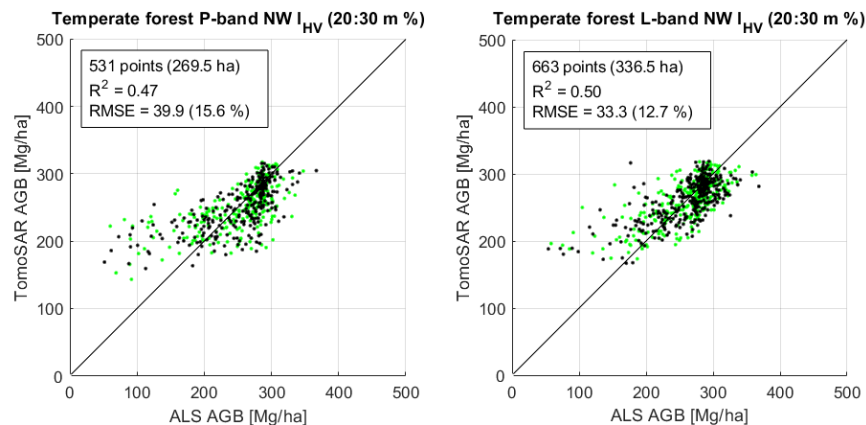
334 9. Sensitivity to forest AGB

335 Figure 13 shows the L-band HV vertical reflectivity profiles for spruce and beech forest from the NW
 336 track bistatic acquisition. The profiles are based on 0.5 ha averages, i.e. the intensity is averaged over
 337 0.5 ha in the horizontal for each height plane, which are then averaged over 20 t/ha AGB intervals. The
 338 curves are colored from low AGB (blue) to high AGB (red), to illustrate the AGB dependence. The

339 changing profiles for spruce and beech show a distinct difference when moving from low to high AGB.
 340 For spruce, the maximum intensity from the canopy is located at about 15-20 m and increases with
 341 AGB. For beech, on the other hand, the location of the maximum intensity increases from about 15 m
 342 to almost 30 m for increasing AGB, whereas the maximum value is almost constant.
 343 The results using one AGB estimation method for temperate forest (a mix of all forest types) at P- and
 344 L-band NW track acquisition is shown in Figure 14. This method uses the fraction of the intensity in
 345 the 20 to 30 m height canopy layer to the total intensity of the vertical profile, for each 0.5 ha data point.
 346 Note that this is a normalized measure, allowing for comparison between points without absolute
 347 intensity calibration. The AGB is estimated through an exponential fit model, $\hat{AGB} = \exp(a_0 + a_1 I_{dB})$
 348 with parameters a_0 and a_1 , estimated using the ALS AGB for half of the points as AGB reference data,
 349 i.e. training data, and the performance is evaluated using the remaining data points. . As seen, the results
 350 at L-band show an R^2 of 0.47 and an RMSE of 39.9 t/ha (15.6 %), while the results at P-band show an
 351 R^2 of 0.50 and an RMSE of 33.3 t/ha (12.7 %).
 352



353 **Fig. 13.** Spruce and beech forest average L-band HV vertical reflectivity profiles for 0.5 ha points in 20
 354 t/ha AGB intervals, from the NW track bistatic acquisition.



356 **Fig. 14.** P- and L-band NW track HV TomoSAR temperate forest (mix of all forest types) AGB
 357 estimation plotted against the reference ALS AGB, using every second point (shown in green) for
 358 training the exponential fit model. This is using the canopy layer fraction method (input is the fraction
 359 of the intensity in the 20 to 30 m canopy layer to the total intensity in the vertical reflectivity profile of
 360 each point).

361

362 With more than 500 data points used for the AGB retrieval at both P- and L-band, the RMSE and R^2
 363 measures are considerably stable. Although, the density of data points is higher at high than at low
 364 AGB, pushing the mean AGB to the higher side of the covered interval. It should also be noted that the
 365 retrieval model tends to weight the estimate towards the mean AGB of the training data points for less
 366 than perfect correlation, minimizing the overall RMSE while overestimating low AGB and
 367 underestimating high AGB. This effect is apparent in the figures, in combination with the fact that a
 368 higher density of high than low AGB data points cause the model to fit high AGB better, in order to
 369 minimize the overall RMSE

370

371 10. Conclusions

372 The TomoSense experiment was conceived to provide key elements in support of the research on future
 373 SAR Missions focused on remote sensing of forested areas, such as the BIOMASS, NISAR, and

374 candidate bistatic missions like Tandem-L. To do that, an extensive data-set was collected comprising
375 P., L-, C- Band data acquired in mono- and bi-static configurations, complemented by detailed
376 terrestrial and aerial Lidar data and forest inventory. Results shown in this paper are only preliminary.
377 Yet, they advocate for the vast range of analysis allowed by this data-set. It was shown that TomoSense
378 provides accurate tomographic imaging of the vegetation at different wavelengths, polarizations, and
379 observation modes, resulting in the possibility to compare Radar and Lidar observables and assess the
380 retrieval of biophysical parameters on a quantitative basis. The entire dataset is free and openly available
381 through ESA for research purposes and can be accessed at <https://earth.esa.int/eogateway/catalog>.
382 Importantly, data are provided in a format that can be directly understood and used by researchers
383 outside the Radar community. For this reason, we deem that TomoSense represents a unique
384 opportunity for the scientific community to better understand the connection between forest biophysical
385 parameters and Radar observables, and use this knowledge for the development of Earth Observation
386 of forested areas.

387

388 **Acknowledgements**

389 This work was funded by the ESA under ESA/ESTEC contract No. 4000127285/19/NL/FF/gp. MD.
390 PW acknowledge capital funding for TLS equipment from UCL Geography and the NERC National
391 Centre for Earth Observation (NCEO). The WUR TLS and UAV-LS campaign was funded by the ESA
392 IDEAS-QA4EO project contract No. 4000128960/19/I-NS.

393

394

395 **References**

- 396 Aghababaei, H., Ferraioli, G., Ferro-Famil, L., Huang, Y., Mariotti D'Alessandro, M., Pascazio, V.,
397 Schirinzi, G., Tebaldini, S. Forest SAR Tomography: Principles and Applications (2020) IEEE
398 Geoscience and Remote Sensing Magazine, 8 (2), art. no. 8995799, pp. 30-45
- 399 Azcueta, M., Tebaldini, S. Potential for Absolute Ionosphere and Clock Correction in Noncooperative
400 Bistatic SAR (2020) IEEE Transactions on Geoscience and Remote Sensing, 58 (1), art. no. 8844297,
401 pp. 363-377
- 402 Blomberg, E., Ulander, L.M.H., Tebaldini, S., Ferro-Famil, L. Evaluating P-Band TomoSAR for
403 Biomass Retrieval in Boreal Forest (2021) IEEE Transactions on Geoscience and Remote Sensing, 59
404 (5), art. no. 9204469, pp. 3793-3804.
- 405 Boni Vicari, M., Disney, M. I., Wilkes, P., Burt, A., Calders, K. and Woodgate, W. (2019) New
406 framework for separating leaf and wood in terrestrial LiDAR point clouds, Methods in Ecology and
407 Evolution, DOI: 10.1111/2041-210X.13144.
- 408 Brede, B., Lau, A., Bartholomeus, H. M., and Kooistra, L. (2017) Comparing RIEGL RiCOPTER UAV
409 LiDAR Derived Canopy Height and DBH with Terrestrial LiDAR, Sensors, 17(10), 2371, doi:
410 10.3390/s17102371.
- 411 Brede, B., Terryn, L., Barbier, N., Bartholomeus, H. M., Bartolo, R., Calders, K., Derroire, G., Krishna
412 Moorthy, S. M., Lau, A., Levick, S. R., Raunonen, P., Verbeeck, H., Wang, D., Whiteside, T., van der
413 Zee, J., & Herold, M. (2022). Non-destructive estimation of individual tree biomass: Allometric models,
414 terrestrial and UAV laser scanning. Remote Sensing of Environment, 280, 113180.
415 DOI:10.1016/j.rse.2022.113180
- 416 Brovkina, O.; Navrátilová, B.; Novotný, J.; Albert, J.; Slezák, L.; Cienciala, E. (2022) Influences of
417 vegetation, model, and data parameters on forest aboveground biomass assessment using an area-based
418 approach. Ecological Informatics 2022(70): 1-12, Article number 101754.

419 Burt, A., Disney, M. I. and Calders, K. (2019) Extracting individual trees from lidar point clouds using
420 treeseq, *Methods in Ecology and Evolution*, <https://doi.org/10.1111/2041-210X.13121>.

421 Disney, M. I. (2018) Terrestrial LiDAR: a 3D revolution in how we look at trees, *New Phytologist*,
422 doi.org/10.1111/nph.15517.

423 Disney, M. I., et al. (2018) Weighing trees with lasers: advances, challenges and opportunities, *Royal*
424 *Society Interface Focus* 8 (2), Special Issue on Royal Society meeting ‘The terrestrial laser scanning
425 revolution in forest ecology’, doi: 10.1098/rsfs.2017.0048.

426 El Moussawi, I., Minh, D.H.T., Baghdadi, N., Abdallah, C., Jomaah, J., Strauss, O., Lavalley, M., Ngo,
427 Y.-N. (2019) Monitoring tropical forest structure using SAR tomography at L- and P-band Remote
428 Sensing, 11 (16), art. no. 1934.

429 Fatoyinbo, T., et al., (2021) The NASA AfriSAR campaign: Airborne SAR and lidar measurements of
430 tropical forest structure and biomass in support of current and future space missions, *Remote Sensing*
431 *of Environment*, 264, art. no. 112533,

432 Frey, O., Morsdorf, F., Meier, E. (2008) Tomographic imaging of a forested area by airborne multi-
433 baseline P-band SAR, *Sensors*, 8 (9), pp. 5884-5896.

434 Ho Tong Minh, D., Le Toan, T., Rocca, F., Tebaldini, S., D'Alessandro, M.M., Villard, L. (2014)
435 Relating P-band synthetic aperture radar tomography to tropical forest biomass, *IEEE Transactions on*
436 *Geoscience and Remote Sensing*, 52 (2), art. no. 6488809, pp. 967-979.

437 Ho Tong Minh, D., Le Toan, T., Rocca, F., Tebaldini, S., Villard, L., Réjou-Méchain, M., Phillips,
438 O.L., Feldpausch, T.R., Dubois-Fernandez, P., Scipal, K., Chave, J. (2016) SAR tomography for the
439 retrieval of forest biomass and height: Cross-validation at two tropical forest sites in French Guiana,
440 *Remote Sensing of Environment*, 175, pp. 138-147.

441 Khati, U., Lavalley, M., Singh, G. (2019) Spaceborne tomography of multi-species Indian tropical
442 forests, *Remote Sensing of Environment*, 229, pp. 193-212.

443 Krisanski, S., Taskhiri, M.S., Gonzalez Aracil, S., Herries, D. and Turner, P., (2021) Sensor Agnostic
444 Semantic Segmentation of Structurally Diverse and Complex Forest Point Clouds Using Deep
445 Learning. *Remote Sensing*, 13(8), p.1413.

446 Mariotti D'Alessandro, M., Tebaldini, S., Quegan, S., Soja, M.J., Ulander, L.M.H., Scipal, K. (2020)
447 Interferometric Ground Cancellation for above Ground Biomass Estimation, *IEEE Transactions on*
448 *Geoscience and Remote Sensing*, 58 (9), art. no. 9033990, pp. 6410-6419.

449 Mariotti D'Alessandro, M., Tebaldini, S. (2019) Digital terrain model retrieval in tropical forests
450 through P-Band SAR tomography, *IEEE Transactions on Geoscience and Remote Sensing*, 57 (9), art.
451 no. 8701518, pp. 6774-6781

452 Mariotti d'Alessandro, M. Tebaldini S., Rocca, F., (2013) Phenomenology of Ground Scattering in a
453 Tropical Forest Through Polarimetric Synthetic Aperture Radar Tomography, *IEEE Transactions on*
454 *Geoscience and Remote Sensing*, vol. 51, no. 8, pp. 4430-4437, Aug. 2013,

455 Mokroš, M., Mikita, T., Singh, A., Tomaščík, J., Chudá, J., Wężyk, P., Kuželka, K., Surový, P.,
456 Klimánek, M., Zięba-Kulawik, K., Bobrowski, R., & Liang, X. (2021). Novel low-cost mobile
457 mapping systems for forest inventories as terrestrial laser scanning alternatives. *International Journal*
458 *of Applied Earth Observation and Geoinformation*, 104, 102512. DOI:10.1016/j.jag.2021.102512

459 Monteith A. R. and Ulander, L. M. H., (2022), A Tower-Based Radar Study of Temporal Coherence
460 of a Boreal Forest at P-, L-, and C-Bands and Linear Cross Polarization, in *IEEE Transactions on*
461 *Geoscience and Remote Sensing*, vol. 60, pp. 1-15, 2022, Art no. 4402315, doi:
462 10.1109/TGRS.2021.3074098.

463 Moreira, A. et al., (2015) Tandem-L: A Highly Innovative Bistatic SAR Mission for Global
464 Observation of Dynamic Processes on the Earth's Surface, *IEEE Geoscience and Remote Sensing*
465 *Magazine*, vol. 3, no. 2, pp. 8-23, June 2015, doi: 10.1109/MGRS.2015.2437353.

466 Orban, A., and Defrere D., Barbier, C., (2021) BelSAR : the first Belgian airborne campaign for L-
467 band, full polarimetric bistatic and interferometric SAR acquisitions over an agricultural site in
468 Belgium, EUSAR 2021; 13th European Conference on Synthetic Aperture Radar, 2021, pp. 1-4.

469 Pardini, M., Papathanassiou, K.P., Lombardini, F. (2018) Impact of dielectric changes on L-band 3-d
470 SAR reflectivity profiles of forest volumes, IEEE Transactions on Geoscience and Remote Sensing, 56
471 (12), art. no. 8424543, pp. 7324-7337.

472 M. Pardini, M. Tello, V. Cazcarra-Bes, K. P. Papathanassiou and I. Hajnsek, "L- and P-Band 3-D SAR
473 Reflectivity Profiles Versus Lidar Waveforms: The AfriSAR Case," in *IEEE Journal of Selected Topics*
474 *in Applied Earth Observations and Remote Sensing*, vol. 11, no. 10, pp. 3386-3401, Oct. 2018, doi:
475 10.1109/JSTARS.2018.2847033.

476 Quegan, S., Le Toan, T., Chave, J., Dall, J., Exbrayat, J.-F., Minh, D.H.T., Lomas, M., D'Alessandro,
477 M.M., Paillou, P., Papathanassiou, K., Rocca, F., Saatchi, S., Scipal, K., Shugart, H., Smallman, T.L.,
478 Soja, M.J., Tebaldini, S., Ulander, L., Villard, L., Williams, M. (2019) The European Space Agency
479 BIOMASS mission: Measuring forest above-ground biomass from space, *Remote Sensing of*
480 *Environment*, 227, pp. 44-60.

481 Raumonon, P., Kaasalainen, M., Åkerblom, M., Kaasalainen, S., Kaartinen, H., Vastaranta, M.,
482 Holopainen, M., Disney, M. and Lewis, P., (2013) Fast automatic precision tree models from
483 terrestrial laser scanner data, *Remote Sensing*, 5(2), pp.491-520.

484 Reigber A., Moreira A., (2000) First demonstration of airborne SAR tomography using multibaseline
485 L-band data, *IEEE Transactions on Geoscience and Remote Sensing*, vol. 38, no. 5, pp. 2142,2152, Sep
486 2000.

487 Reigber, A., Prats P., and Mallorqui, J. J., (2006) Refined estimation of time-varying baseline errors in
488 airborne SAR interferometry, *IEEE Geoscience and Remote Sensing Letters*, vol. 3, no. 1, pp. 145-
489 149, Jan. 2006.

490 Scipal, K. and Davidson, M., (2017) The SAOCOM-CS mission: ESA's first bistatic and tomographic
491 L-band mission, 2017 IEEE International Geoscience and Remote Sensing Symposium (IGARSS),
492 2017, pp. 123-124.

493 Siegmann, B., et al: (2019) The High-Performance Airborne Imaging Spectrometer HyPlant—From
494 Raw Images to Top-of-Canopy Reflectance and Fluorescence Products: Introduction of an Automatized
495 Processing Chain, *Remote Sens.* 2019, 11, 2760.

496 Soja, M.J., Quegan, S., d'Alessandro, M.M., Banda, F., Scipal, K., Tebaldini, S., Ulander, L.M.H.
497 (2021) Mapping above-ground biomass in tropical forests with ground-cancelled P-band SAR and
498 limited reference data, *Remote Sensing of Environment*, 253, art. no. 112153.

499 Tebaldini, S., Ho Tong Minh, D., Mariotti d'Alessandro, M., Villard, L., Le Toan, T., Chave, J.
500 (2019) The Status of Technologies to Measure Forest Biomass and Structural Properties: State of the
501 Art in SAR Tomography of Tropical Forests, *Surveys in Geophysics*, 40 (4), pp. 779-801.

502 Tebaldini, S., Rocca, F., Mariotti D'Alessandro, M., Ferro-Famil, L. (2016) Phase calibration of
503 airborne tomographic SAR data via phase center double localization, *IEEE Transactions on*
504 *Geoscience and Remote Sensing*, 54 (3), art. no. 7308057, pp. 1775-1792.

505 Tebaldini S., Ferro-Famil, L. (2017) SAR tomography from bistatic single-pass interferometers, 2017
506 IEEE International Geoscience and Remote Sensing Symposium (IGARSS), 2017, pp. 133-136,

507 Tello, M., Cazcarra-Bes, V., Pardini, M., Papathanassiou, K. (2018) Forest structure characterization
508 from SAR tomography at L-band, *IEEE Journal of Selected Topics in Applied Earth Observations and*
509 *Remote Sensing*, 11 (10), art. no. 8457291, pp. 3402-3414.

510 Toraño Caicoya, A., Pardini, M., Hajnsek, I., Papathanassiou, K. (2015) Forest Above-Ground Biomass
511 Estimation From Vertical Reflectivity Profiles at L-Band, *IEEE Geoscience and Remote Sensing*
512 *Letters*, 12 (12), art. no. 7305772, pp. 2379-2383

513 Villa, A., Iannini, L., Giudici, D., Monti-Guarnieri, A., Tebaldini, S. (2015) Calibration of SAR
514 polarimetric images by means of a covariance matching approach IEEE Transactions on Geoscience
515 and Remote Sensing, 53 (2), art. no. 6834807, pp. 674-686.

516 Wilkes, P., Lau, A., Disney, M., Calders, K., Burt, A., de Tanago, J.G., Bartholomeus, H., Brede, B.
517 and Herold, M., (2017) Data acquisition considerations for terrestrial laser scanning of forest
518 plots, Remote Sensing of Environment, 196, pp.140-153.

519 Wilkes, P., Disney, M.I., Armston, J., Bartholomeus, H., Bentley, L.P., Brede, B., Burt, A., Calders,
520 K., Chavana-Bryant, C., Clewley, D. and Duncanson, L. (2022) TLS2trees: a scalable tree
521 segmentation pipeline for TLS data. *bioRxiv*; <https://doi.org/10.1101/2022.12.07.518693>

522 Wutzler, T., Wirth, C. and Schumacher, J. (2008) Generic biomass functions for Common beech
523 (*Fagus sylvatica*) in Central Europe: predictions and components of uncertainty, Canadian Journal of
524 Forest Research, 38(6), pp. 1661–1675 (2008) doi: 10.1139/X07-194

525 Yu, Y., d'Alessandro, M.M., Tebaldini, S., Liao, M. (2020) Signal processing options for high
526 resolution SAR tomography of natural scenarios Remote Sensing, 12 (10), art. no. 1638, .

527 Zianis, D., Muukkonen, P., Makipaa, R., & Mencuccini, M. (2005). Biomass and stem volume
528 equations for tree species in Europe. *Silva Fennica monographs*, (4), 1-2,5-63